Precision Landing Navigation Performance of Human-Scale Lunar and Mars Landers

Rafael A. Lugo,[1] Robert A. Williams,[2] Soumyo Dutta,[3] and
Alicia Dwyer Cianciolo[4]
NASA Langley Research Center, Hampton, Virginia, 23681, USA

Po-Ting Chen[5]
Jet Propulsion Laboratory, Pasadena, California, 91109, USA

To meet the unique challenges of crewed Lunar and Mars precision landings, NASA's Safe and Precise Landing Integrated Capabilities Evolution project has worked to advance autonomous spacecraft navigation by increasing the technology readiness level of key deorbit, entry, descent, and landing systems, including navigation sensors. Different sensors and their effects on overall system performance are evaluated using six-degree-of-freedom simulations with physics-based engineering models that capture the relevant vehicle systems and environmental effects. Building on an existing simulation framework, this work demonstrates how improved modeling fidelity enables rapid and detailed assessment of various navigation sensors on human-scale Lunar and Mars landing vehicles using NASA reference architectures.

I. Introduction

Recent NASA studies of crewed missions to the Moon and Mars have highlighted the need for an autonomous safe and precise landing capability. The payload and mass requirements for these human-scale missions are orders of magnitude higher than previous robotic-scale missions, and numerous challenges must be addressed and technologies matured before these types of landings become feasible, including in the area of spacecraft navigation. The Safe and Precise Landing Integrated Capabilities Evolution (SPLICE) project is tasked with advancing autonomous spacecraft navigation through multiple areas of research and development. A crucial aspect of this effort is increasing the technology readiness level (TRL) of key deorbit, entry, descent, and landing (D/EDL) guidance, navigation, and control (GN&C) systems. Detailed six degree-of-freedom (6DOF) physics-based engineering simulations are used to aid in evaluation of these systems in an integrated performance sense [1]. Different navigation sensors and their effects on overall system performance are evaluated using these simulations.

In this work, an update [1] is presented. Updates to the models built to represent navigation sensors and other spacecraft systems are described, and emphasis is placed on how improved modeling fidelity enables rapid and detailed assessment of the overall integrated system performance.

II. Applications: Human-Scale Landings

The navigation performance of two case studies will be analyzed in this work: a human-scale Lunar landing and a human-scale Mars landing.

---

[1] Aerospace Engineer, Atmospheric Flight and Entry Systems Branch, AIAA Member.
[2] Research Computer Scientist, Atmospheric Flight and Entry Systems Branch.
[3] Aerospace Engineer, Atmospheric Flight and Entry Systems Branch, AIAA Senior Member.
[4] Aerospace Engineer, Atmospheric Flight and Entry Systems Branch, AIAA Senior Member.
[5] Member of Technical Staff, Guidance and Control Section.

A. Human-Scale Lunar Landing

The Artemis program began in 2019 with a directive to return humans to the Moon by 2024 [2]. To that end, NASA awarded contracts in May 2020 to three companies to design and build the integrated Lunar lander vehicle [3]. During this time, NASA designed and maintained a government reference design for a Lunar lander that is continuously refined in parallel with the efforts from the private sector.

1. Deorbit, Descent, and Landing Vehicle

The government reference design used in the present study is from an abbreviated NASA Design Analysis Cycle (Mini-DAC) that focused a storable propellant system that does not rely on cryogenics, increasing the readiness of the design for 2024 [4]. The design is a three-element architecture with a disposable Transfer Element (TE), Descent Element (DE), and Ascent Element (AE). The final version of this manuscript will include more detailed information regarding the relevant vehicle systems.

2. Concept of Operations

The DDL concept of operations of the government reference design for the Artemis Lunar lander is shown in Fig. 1. DDL begins in the 100 km circular parking orbit. The deorbit burn places the vehicle in an intermediate 100x15.24 km orbit, and powered descent begins at periapsis with braking burn 1 performed by the TE. When the TE propellant is depleted, the TE is jettisoned (impact is nominally downrange from the targeted landing site), and braking burn 2 is initiated after a 40 s coast. The braking burns are designed to reduce the vehicle velocity as efficiently as possible. The vehicle then transitions to the approach phase, during which the vehicle orientation is adjusted such that landing navigation sensors and pilot view angles are accommodated for hazard detection and avoidance. During this phase, vehicle thrust is controlled such that once the vehicle is over the landing site, horizontal velocity is nullified. Note that the "braking" and "approach" nomenclature is a holdover from the Apollo Moon landings. Terminal descent begins at an altitude of 200 m, and the vehicle velocity is reduced further such that the main engines cut off an altitude of 1 m and a velocity of 1 m/s.
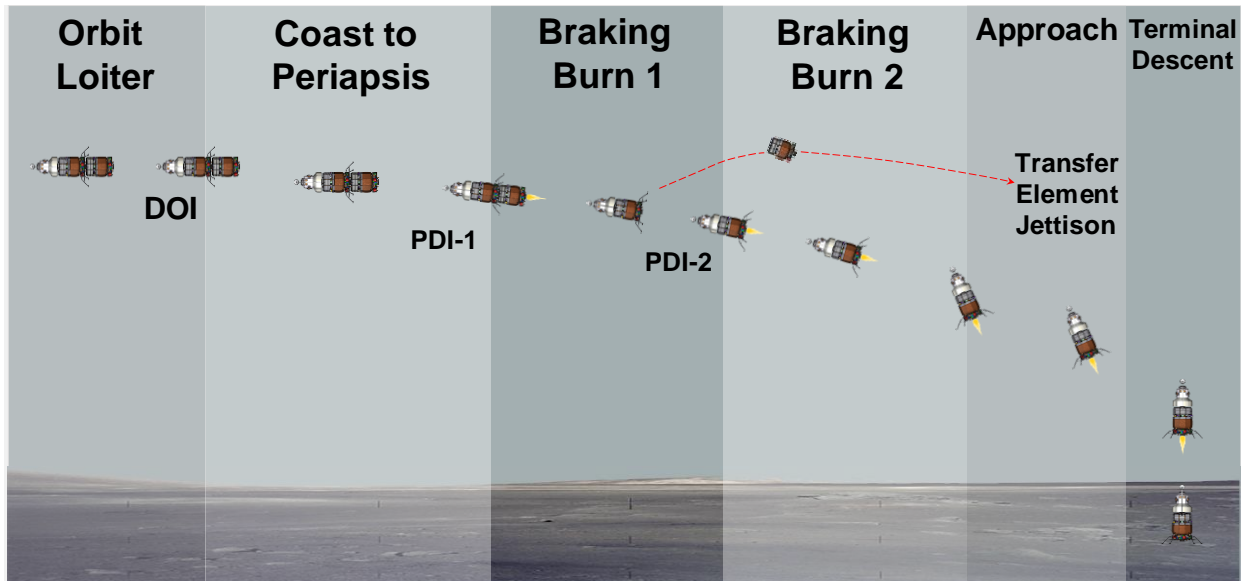

Fig. 1 Artemis Lunar lander DDL concept of operations, government reference design.

B. Human-Scale Mars Landing

A particularly challenging case of precision landing is that of a human-scale Mars lander. The current NASA architecture includes landing 20 t payloads to an altitude of 0 km with a landing accuracy of 50 m [5]. While state, vehicle, and navigation uncertainties dominate dispersion assessments for Moon landings, Mars landings are dominated by navigation and atmospheric uncertainties. Mars atmospheric variability and forecasting uncertainty means that the entry vehicle and GN&C system must be robust enough to accommodate landing during any time in the Mars year, including dust storm season. These effects, as well as the high payload mass requirements, are some of the main drivers for EDL and precision landing technology development.

1. Deorbit, Entry, Descent, and Landing Vehicle

The human-scale Mars entry vehicle utilizes a hypersonic inflatable aerodynamic decelerator (HIAD) [5]. Control of the vehicle dynamics during entry is provided by four aerodynamic flaps, shown in Fig. 3 (note the lower flap is partially deployed). This configuration enables the use of direct force control (DFC), which takes advantage of the decoupled angle of attack and sideslip control to manage downrange and crossrange control during entry. Control of the vehicle dynamics during powered descent is provided by eight 100 kN supersonic retropropulsion (SRP) main engines arranged in a doublet configuration. SRP is an approach that uses powered flight rather than more traditional parachute to reduce velocity during the descent and landing phases of EDL.
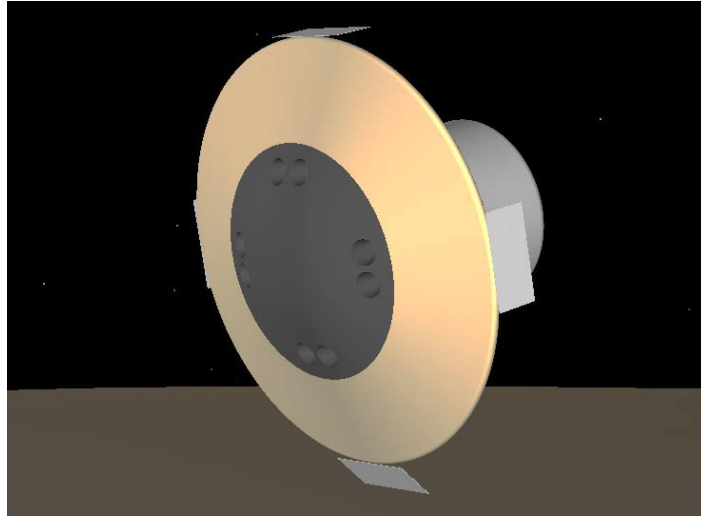

Fig. 2 Representation of the HIAD entry vehicle.

2. Concept of Operations

The EDL concept of operations is shown in Fig. 4. The crewed entry vehicle performs a deorbit burn at apoapsis of a 1 Sol polar orbit (33793 km apoapsis altitude by 250 km periapsis altitude). The polar orbit was chosen for the study because it permits access to any landing site on Mars. After the deorbit burn, the vehicle coasts until atmospheric entry interface (125 km altitude), at which point the simulation atmosphere and aerodynamic models are activated. The guidance and control algorithms are activated when the sensed vehicle acceleration reaches 0.15 g's. Throughout entry, DFC is utilized by the guidance, which commands angles of attack and sideslip to control downrange and crossrange errors, respectively. At powered descent initiation (PDI), the main engines are activated and the vehicle begins the powered descent main phase using an augmented gravity turn through the use of differentially throttled main engines. The powered descent terminal phase occurs when the vehicle is directly over the landing site and descends vertically at a constant velocity of 2.5 m/s for 5 s.
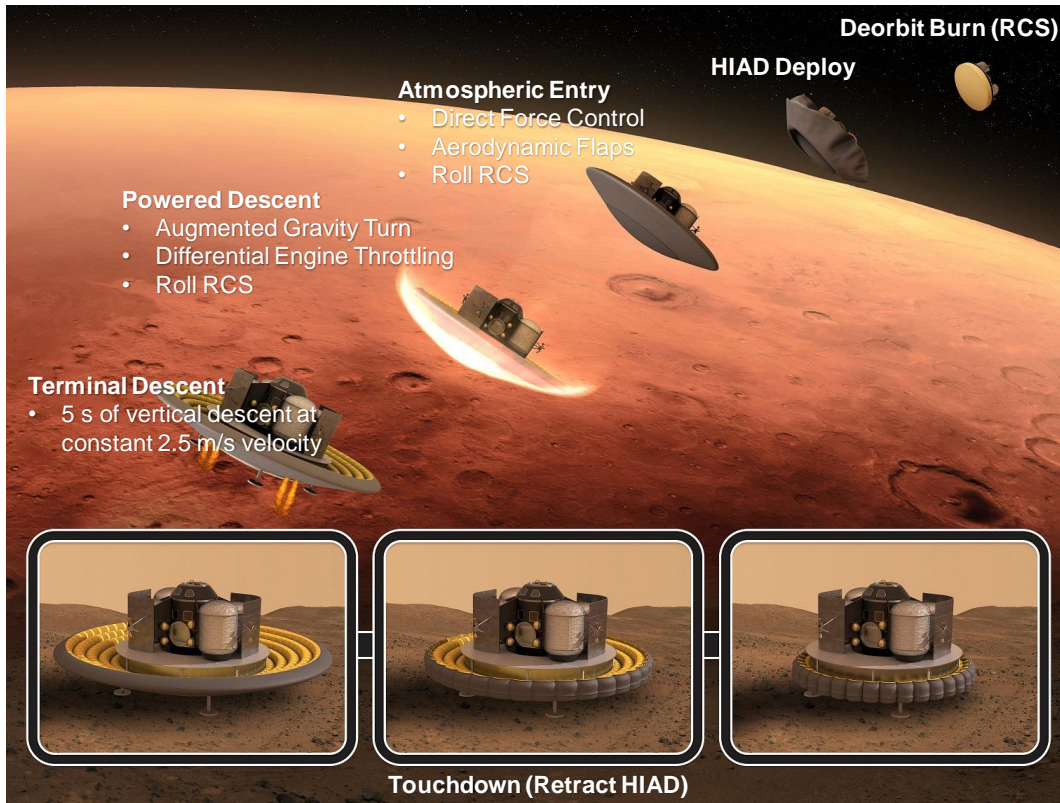
Fig. 3 Human-scale Mars EDL with HIAD vehicle.

III. Simulation Framework and System Modeling

The D/EDL case studies described in Section III are simulated using the 6DOF framework presented in [1]. This framework consists of generalized, modular, and user-configurable engineering models of various vehicle systems for the Program to Optimize Simulated Trajectories II (POST2). The suite of models includes guidance, navigation, and control algorithms, as well as aerosurface and propulsion system actuators.

A. Guidance and Control

Guidance and control algorithms differ between the two case studies. However, both cases are driven by the same simulation framework, and simply call the appropriate algorithms as needed.

1. *Human-Scale Lunar Landing*

The Artemis lander uses the Apollo powered descent guidance as formulated in [6]. During deorbit and coast phases, attitude control is provided by reaction control system (RCS) thrusters. Attitudes and angular rate commands are provided by a generalized three-axis phase-plane RCS controller to generate desired moment commands, which are then translated by the phase-plane controller into RCS jet firings.

During powered descent, RCS is used for roll control only. The roll command is set to zero and passed through a generalized phase-plane RCS controller to generate desired moment commands, which are then translated by the phase-plane controller into jet firings. Pitch and yaw control are provided by the three DE main engines. Pitch and yaw commands are passed through a proportional-integral-derivative (PID) controller to generate desired angular acceleration commands, which are then in turn passed through a TVC allocator to determine jet firings.

2. *Human-Scale Mars Landing*

The human-scale Mars lander uses a generalized numerical predictor-corrector targeting guidance (NPCG) for entry, descent, and landing [7]. During deorbit and coast phases, attitude control is provided by RCS thrusters and the same generalized three-axis phase-plane controller used in the Artemis Lunar lander case.

During powered descent, RCS is reduced to bank only and the command set to zero, and angle of attack and sideslip control are provided by differentially throttling the eight main engines.

B. Navigation
The simulation framework includes a suite of spacecraft navigation models that are generalized to the extent that they can be used to simulate sensors of varying quality for a variety of mission scenarios. The full sensor suite is described in [1] and includes engineering and behavioral models of an IMU, star tracker, altimeter, velocimeter, navigational Doppler light detection and ranging (LIDAR, NDL), terrain-relative navigation (NDL), hazard detection (HD), ground update/Deep Space Network (DSN), and a flush air data system (FADS). This section will detail new or improved model capability since the publication of [1].

1. Multi-Mode Extended Kalman Filter
An extended Kalman Filter provided by the NASA Engineering & Safety Center (NESC) was implemented in the simulation framework [8]. This multi-mode EKF (MEKF) is designed as an easily configurable navigation filter that can be used for various mission scenarios, including Lunar DDL and Mars EDL. The MEKF includes built-in navigation models for an IMU, star tracker, altimeter, and velocimeter. The MEKF has been augmented by adding similar models for TRN, NDL, and ground station updates.

2. Terrain-Relative Navigation
The final manuscript will provide a description of the updates to the TRN sensor model.

3. Navigational Doppler LIDAR
An NDL model provided [9] was implemented in the simulation. The final manuscript will provide a description of this model.

C. Monte Carlo Analysis
Monte Carlo analyses were performed using the dispersions listed in Table 3. The 'dusttau' listed is a measure of the dust loading in the atmosphere and has a significant impact on the density profile. Therefore, it is included in the Monte Carlos in addition to the nominal dispersions.

Table 1   Monte Carlo Dispersions.

Category	Parameter	Dispersion (Moon)	Dispersion (Mars)	Distribution
Initial Conditions	Deorbit burn execution	0.135 m/s 3σ	0.135 m/s 3σ	normal
	Uncorrelated state covariance	0.03º 3σ for angles, 0.03 km 3σ for altitudes	0.03º 3σ for angles, 0.03 km 3σ for altitudes	normal
Atmosphere	Density	N/A	MarsGRAM	--
	Winds	N/A	MarsGRAM	--
	Dusttau	N/A	0.1:0.9	uniform
Aerodynamics	Aerodatabase uses coefficient multipliers and adders for different aerodynamic regimes based on CFD, wind tunnel tests, and flight data from similar shapes	N/A	--	--
Propulsion	Peak thrust	Scale factor: 1% 3σ	Scale factor: 1% 3σ	normal
	Peak Isp	Scale factor: 1% 3σ	Scale factor: 1% 3σ	normal
	Start lag time	0.0:0.2 s	0.0:0.2 s	uniform
	Startup transient rate	Scale factor: 1% 3σ	Scale factor: 1% 3σ	normal
	Main phase response rate	Scale factor: 1% 3σ	Scale factor: 1% 3σ	normal
Mass	Mass	500 kg 3σ	500 kg 3σ	normal
	Center of gravity	0.05 m 3σ	0.05 m 3σ	normal
	Moments of inertia	5% kg-m^2 3σ	5% kg-m^2 3σ	normal

IV. Results

Initial results from the POST2 simulation of the Artemis lander are shown in Fig. 4. First, a case with a perfect IMU results in the navigation position error exceeding 3000 km by touchdown. By adding Deep Space Network (DSN), star tracker, and TRN updates, the final navigation position error is driven down to less than four meters. Navigation velocity errors are also improved by an order of magnitude. Note Fig. 4 shows nominal trajectories, that is, trajectories without Monte Carlo dispersion errors applied.

The final manuscript will include additional cases with different sensors, as well as Monte Carlo results, analysis, and interpretation.
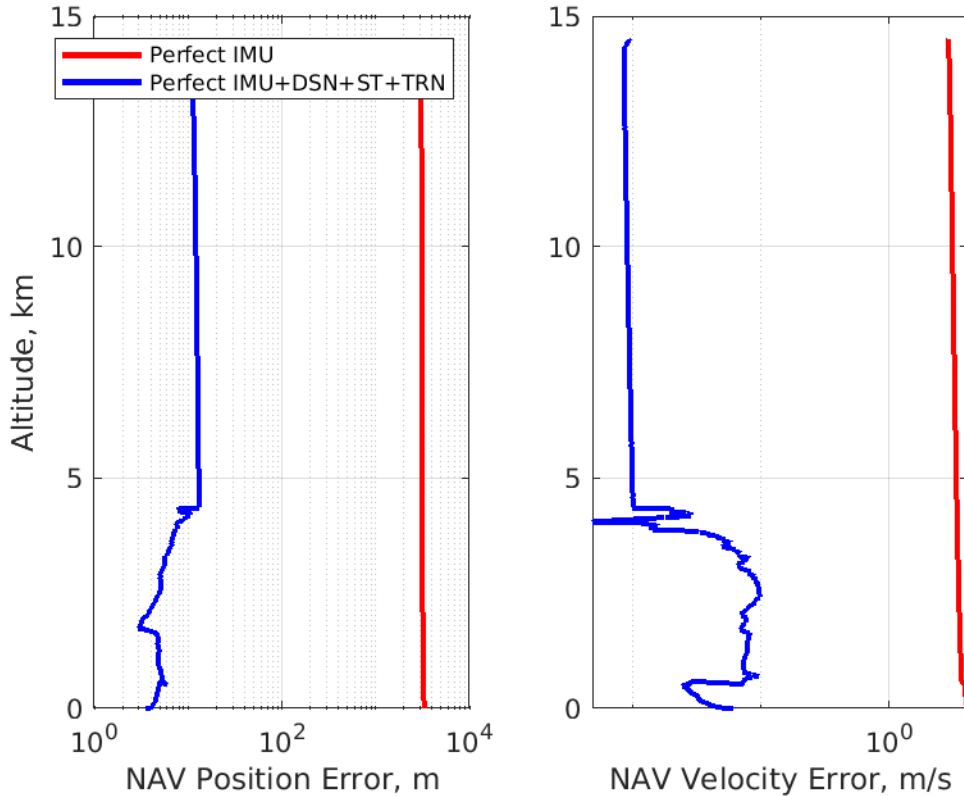

Fig. 4 Navigation position and velocity errors, Artemis Lander.

References

[1] Cianciolo, A. D., Dutta, S., Lugo, R. A., Williams, R. A., and Chen, P., "A Simulation Framework for Precision Landing and Hazard Avoidance Technology Assessments," AIAA 2020-0366.

[2] Dunbar, B., "What is Artemis?," [website], URL: https://www.nasa.gov/what-is-artemis [retrieved 22 May 2020].

[3] Potter, S., "NASA Names Companies to Develop Human Landers for Artemis Moon Missions," [online article], URL: https://www.nasa.gov/press-release/nasa-names-companies-to-develop-human-landers-for-artemis-moon-missions [retrieved 22 May 2020].

[4] Craig, A. S., Hannan, M. R. , Lugo, R. A. , Burke, L. M., Condon, G. L., Mahajan, B., Belanger, B. L., Summers, A. W., Pei, J., May, Z. D., "Human Landing System Storable Propellant Architecture: Mission Design, Guidance, Navigation, and Control," AAS Preprint.

[5] Cianciolo, A. D., Korzun, A., Edquist, K., Samareh, J., Sostaric, R., Calderon, D., and Garcia, J. A., "Human Mars Entry, Descent, and Landing Architecture Study: Phase 3 Summary," AIAA 2020-1509.

[6] Sostaric, R. R., and Rea, J. R., "Powered Descent Guidance Methods for the Moon and Mars," AIAA 2005-6287.

[7] Lugo, R. A., Powell, R. W., and Cianciolo, A. D., "Overview of a Generalized Numerical Predictor-Corrector Targeting Guidance with Application to Human-Scale Mars Entry, Descent, and Landing," AIAA 2020-0846.

[8] Bishop, R. H., "NASA Engineering and Safety Center Simulation Framework for Rapid EDL: Multi-Mode Extended Kalman Filter," V1.0, Oct. 2010 (unpublished).

[9] Gragossian, A., Pierrottet, D., Estes, J., Barnes, B. W., Amzajerdian, F., and Hines, G. D., "Navigation Doppler Lidar Performance at High Speed and Long Range," AIAA 2020-0369.